

## Modeling, measurement, and 3-D equilibrium reconstruction of the bootstrap current in the Helically Symmetric Experiment

J. C. Schmitt, J. N. Talmadge, D. T. Anderson, and J. D. Hanson

Citation: *Physics of Plasmas* **21**, 092518 (2014); doi: 10.1063/1.4895899

View online: <http://dx.doi.org/10.1063/1.4895899>

View Table of Contents: <http://scitation.aip.org/content/aip/journal/pop/21/9?ver=pdfcov>

Published by the *AIP Publishing*

---

### Articles you may be interested in

[Non-axisymmetric equilibrium reconstruction of a current-carrying stellarator using external magnetic and soft x-ray inversion radius measurements](#)

*Phys. Plasmas* **22**, 122509 (2015); 10.1063/1.4938031

[Profile stiffness measurements in the Helically Symmetric experiment and comparison to nonlinear gyrokinetic calculationsa\)](#)

*Phys. Plasmas* **22**, 056107 (2015); 10.1063/1.4921146

[Gyrokinetic turbulent transport simulation of a high ion temperature plasma in large helical device experiment](#)

*Phys. Plasmas* **19**, 042504 (2012); 10.1063/1.4704568

[Extended estimations of neoclassical transport for the TJ-II stellarator: The bootstrap current](#)

*Phys. Plasmas* **18**, 102507 (2011); 10.1063/1.3649928

[H  \$\alpha\$  measurements and neutral particle transport in Heliotron J](#)

*Rev. Sci. Instrum.* **77**, 10E527 (2006); 10.1063/1.2347621

---



**PFEIFFER VACUUM**

## VACUUM SOLUTIONS FROM A SINGLE SOURCE

Pfeiffer Vacuum stands for innovative and custom vacuum solutions worldwide, technological perfection, competent advice and reliable service.

# Modeling, measurement, and 3-D equilibrium reconstruction of the bootstrap current in the Helically Symmetric Experiment

J. C. Schmitt,<sup>1,a)</sup> J. N. Talmadge,<sup>1</sup> D. T. Anderson,<sup>1</sup> and J. D. Hanson<sup>2</sup>

<sup>1</sup>Department of Electrical and Computer Engineering, University of Wisconsin-Madison, Madison, Wisconsin 53706, USA

<sup>2</sup>Department of Physics, Auburn University, Auburn, Alabama 36849, USA

(Received 20 June 2014; accepted 4 September 2014; published online 26 September 2014)

The bootstrap current for three electron cyclotron resonance heated plasma scenarios in a quasisymmetric stellarator (the Helically Symmetric Experiment) are analyzed and compared to a neoclassical transport code PENTA. The three conditions correspond to 50 kW input power with a resonance that is off-axis, 50 kW on-axis heating and 100 kW on-axis heating. When the heating location was moved from off-axis to on-axis with 50 kW heating power, the stored energy and the extrapolated steady-state current were both observed to increase. When the on-axis heating power was increased from 50 kW to 100 kW, the stored energy continued to increase while the bootstrap current slightly decreased. This trend is qualitatively in agreement with the calculations which indicate that a large positive electric field for the 100 kW case was driving the current negative in a small region close to the magnetic axis and accounting for the decrease in the total integrated current. This trend in the calculations is only observed to occur when momentum conservation between particle species is included. Without momentum conservation, the calculated bootstrap current increases monotonically. We show that the magnitude of the bootstrap current as calculated by PENTA agrees better with the experiment when momentum conservation between plasma species is included in the calculation. The total current was observed in all cases to flow in a direction to unwind the transform, unlike in a tokamak in which the bootstrap current adds to the transform. The 3-D inductive response of the plasma is simulated to predict the evolution of the current profile during the discharge. The 3-D equilibrium reconstruction code V3FIT is used to reconstruct profiles of the plasma pressure and current constrained by measurements with a set of magnetic diagnostics. The reconstructed profiles are consistent with the measured plasma pressure profile and the simulated current profile when the reconstruction is constrained by the measured data from a diagnostic array that is internal to the vacuum chamber. © 2014 AIP Publishing LLC.

[<http://dx.doi.org/10.1063/1.4895899>]

## I. INTRODUCTION

The correct modeling of the bootstrap current is critical for toroidal fusion experiments. The evolution of this current can take several seconds in present day experiments and will evolve on the timescale of minutes in ITER. During that time the equilibrium will be continuously changing. The bootstrap current has a large effect in stellarators, especially for quasi-axisymmetric stellarators.<sup>1</sup> The understanding of the bootstrap current and its temporal behavior is necessary for the proper operation of the W7-X divertor where the goal is to keep the edge transform fixed to maintain a natural island divertor.<sup>2</sup>

Neoclassical transport quantities, such as the ion and electron parallel flows that make up the bootstrap current, are calculated for nonaxisymmetric geometries using the linearized drift kinetic equation. The DKES code<sup>3</sup> (Drift Kinetic Equation Solver) is commonly used in stellarators to calculate neoclassical transport coefficients. However, it makes two important assumptions that significantly reduce

the dimensionality and complexity of the problem: (1) the  $E \times B$  drift is incompressible, which allows for a monoenergetic treatment and the particle velocity becomes an input parameter and (2) only the pitch-angle scattering part of the collision operator is used so that momentum is not conserved. In recent years, several approaches<sup>4-6</sup> have appeared, which take the monoenergetic coefficients calculated by a code like DKES and correct for momentum conservation. In this paper, we use the PENTA code<sup>7,8</sup> to perform the momentum correction, which is based on the Sugama and Nishimura approach. The importance of momentum correction to calculations of the bootstrap current has not been demonstrated experimentally. Momentum correction in calculations of the predicted total integrated bootstrap current in Wendelstein 7-X show that the effect is 15% for the low-mirror configuration and 31% for the high-mirror case.<sup>6</sup>

For typical plasma parameters during Electron Cyclotron Resonant Heating (ECRH) in stellarators, the operating density is low, the electrons and ions are not coupled strongly,  $T_e$  is often much greater than  $T_i$ , and the two species may be in different collisionality regimes. It has been shown in Ref. 9 that the geometric factor in the expression for the bootstrap current that multiplies the thermodynamic forces is a function

<sup>a)</sup>Present address: Princeton Plasma Physics Laboratory, P.O. Box 451, Princeton, New Jersey 08543, USA.

of the magnetic field configuration and the collisionality. This factor can be different for ions and electrons and gives rise to a dependence of the bootstrap current on the radial electric field for stellarators that is absent in axisymmetric devices. In tokamaks, for example, this geometric factor is the same for all species and for all collisionalities such that when the parallel flow for the individual species, which is dependent on  $E_r$ , are added together the  $E_r$  contribution to the bootstrap current cancels out identically. This result is true for the diamagnetic and Pfirsch-Schlüter currents in both symmetric and nonsymmetric devices. This model was first applied to calculate the bootstrap current in LHD<sup>10</sup> in which it was shown for a model calculation typical of an ECRH plasma that a large radial electric field leads to a reduction in the bootstrap current compared to  $E_r = 0$ , while a negative  $E_r$  has the opposite effect. Experimental evidence of the  $E_r$  effect on the bootstrap current in stellarators is sparse. Heliotron-J reported evidence of a reversal of the bootstrap current at low density possibly attributed to a large positive electric field, although density, temperature, and potential profiles were absent.<sup>11</sup>

The Pustovitov-Shafranov<sup>12</sup> and Strand-Houlberg<sup>13</sup> model, which includes the non-axisymmetric geometric effects of a 3-D plasma, was developed to simulate the current diffusion in a stellarator. Ignoring the 3-D shape of the plasma neglects additional coupling between the toroidal and poloidal magnetic fluxes. The result for the Helically Symmetric Experiment (HSX), which will be shown in this paper, is that the decay rate of the current diffusion is underestimated when the plasma column is assumed to be axisymmetric, even when other values are held the same (conductivity, sources of current, etc.).

In addition to the correct steady-state and temporal modeling of the bootstrap current, the reconstruction of the equilibrium plasma pressure and current profiles is important for toroidal plasma devices. The reconstruction provides information about the shape and location of the magnetic surfaces and the rotational transform profile. This information is used in subsequent calculations of the stability and transport properties and for the interpretation of other diagnostics. EFIT<sup>15</sup> is a standard tool for reconstructing the equilibrium of 2-D axisymmetric devices, but it is inadequate for 3-D systems. There is an increasing emphasis on 3-D physics including the modeling of resonant magnetic perturbation (RMP) coils on tokamaks, quasihelicity states in reversed-field pinches (RFPs), and stellarators, both conventional and optimized.<sup>16</sup> The STELLOPT code was used to reconstruct the 3-D equilibrium of a high beta discharge in W7-AS.<sup>17</sup> Similarly, the V3FIT<sup>18</sup> code was developed to calculate the signals for a set of diagnostics due to the plasma and coil currents of a VMEC equilibrium solution,<sup>19</sup> which is valid for axisymmetric and non-axisymmetric 3-D systems. This information is used to perform equilibrium reconstructions by minimizing the mismatch between the modeled and experimental diagnostic signals.

In this paper, Sec. II describes the experiment, the diagnostics, and the modeling. Section III gives the experimental results, and Sec. IV contains a summary and discussion.

## II. EXPERIMENT, DIAGNOSTICS, AND MODELING

### A. HSX

The HSX stellarator<sup>20</sup> is a four-field period quasisymmetric stellarator with a modular coilset that generates a magnetic field such that  $|B|$  is approximately constant in a helical direction on a flux surface. The magnetic field spectrum on a flux surface in a stellarator is given by<sup>21</sup>

$$\frac{B}{B_0} = \sum_{n,m} b_{n,m} \cos(n\zeta - m\theta), \quad (1)$$

where the toroidal and poloidal angles are given by  $\zeta$  and  $\theta$ , respectively, and  $n$  and  $m$  are the toroidal and poloidal mode numbers. The dominant magnetic spectral term in HSX is the  $n = 4, m = 1$  component which accounts for the property of being quasihelically symmetric (QHS). The toroidal curvature component ( $n = 0, m = 1$ ) for a QHS device is very small. A property of a QHS machine is that it has a high effective transform, given by  $t_{eff} = n - m\iota \approx 3$ , where the nominal transform  $\iota$  ranges from 1.04 in the core to 1.12 at the edge. This high effective transform results in reduced orbit drifts for passing particles.<sup>22</sup> The high effective transform is also responsible for reduced Pfirsch-Schlüter and bootstrap currents. The Pfirsch-Schlüter is expressed as<sup>23</sup>

$$\mathbf{J}_{PS} = \frac{\mathbf{B}}{B_0^2} \frac{dp}{d\Phi} \sum_{(n,m) \neq (0,0)} \frac{nI + mF}{n - m\iota} \delta_{n,m} \cos(n\zeta - m\theta), \quad (2)$$

where  $\delta_{n,m}$  is the spectral component when  $1/B^2$  is expanded in a Fourier series.  $I$  is the toroidal current enclosed by a flux surface,  $F$  is the poloidal current exterior to a flux surface,  $p$  is the plasma pressure, and  $\Phi$  is the enclosed toroidal flux. The Pfirsch-Schlüter current has the unique property of rotating with the helical  $|B|$  contours as a function of the toroidal angle. This dependence upon toroidal angle is demonstrated in Fig. 1, where contours of the Pfirsch-Schlüter current density are shown at three different toroidal angles. The region of ( $\mathbf{J}_{PS} < 0$ ) rotates from the inboard side of the plasma column near the 1/2 field period location to the outboard side near the 1/6 field period location. A sketch of the magnetic field generated by this current distribution is shown in the left contour plot of the figure.

Likewise, the bootstrap current for a magnetic configuration dominated by a single harmonic is<sup>24</sup>

$$J_B = 1.46 \frac{g}{B_0} \frac{m\sqrt{b_{n,m}}}{n - m\iota} \left[ 1.67(T_e + T_i) \frac{dn}{d\Phi} + 0.47n \frac{dT_e}{d\Phi} - 0.29n \frac{dT_i}{d\Phi} \right]. \quad (3)$$

The  $g$  in this expression is the poloidal current outside the flux surface times the permeability of free space,  $\mu_0$ . In the expression above, the radial electric field dependence for a nonsymmetric configuration is ignored. Compared to a tokamak where the spectrum is dominated by toroidal curvature, the bootstrap current is reduced by the effective transform.

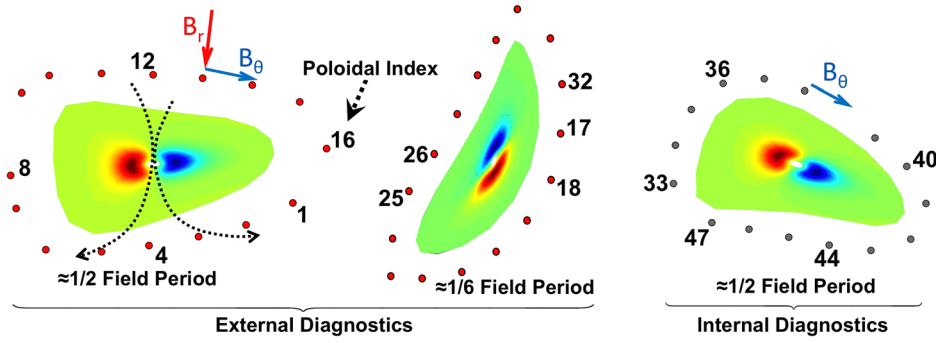


FIG. 1. Contour plot of the Pfirsch-Schlüter current density and the location of the magnetic diagnostic sets at three toroidal locations along a field period. Red contours indicate current directed into the plane ( $J_{PS} < 0$ ) while the blue contours indicate current directed out of the plane ( $J_{PS} > 0$ ). The black arrows on the left plot indicate the dipole magnetic field generated by this current density.

Also, the bootstrap current in a QHS device is in the opposite direction compared to a tokamak and acts to decrease the rotational transform. Note too that a decreasing rotational transform actually increases the effective transform, but only slightly because in most cases  $n > m$ . Plasmas in HSX are heated with up to 100 kW ECRH provided by a 28 GHz gyrotron configured for 1st-harmonic O-mode operation. The magnetic field strength on-axis is 1.0 T. Electron temperatures can reach as high as 2.5 keV in the core, depending on the plasma density. Ion temperatures are in the range of 40–65 eV.

## B. Diagnostics

The magnetic diagnostic set includes a diamagnetic loop, two Rogowski coils, and three arrays of coils located at three separate toroidal locations as shown in Figure 2. The diamagnetic loop is a 10-turn loop installed on the inside of the vacuum vessel and measures changes to the enclosed toroidal flux at a nearly constant toroidal plane. One Rogowski coil is located outside the vacuum chamber and the other is inside of a reentrant flexible thin-walled stainless steel hose interior to the vacuum vessel. They are both near the same toroidal location. The three coil arrays are shown in Figure 1. Two of the arrays of the coils are outside the vacuum chamber separated by 1/3 of a field period. Each external array has 16 coils spaced poloidally about the plasma that measure changes in the local magnetic field vector in their own local orthogonal coordinate system. The third array is interior to the vacuum vessel in a reentrant hose and has

15 coils that measure the poloidal component of the magnetic field only.

The difference between the internal and external Rogowski coil measurements indicate that a small net toroidal current is driven in the vacuum vessel ( $\sim 10$  A) at the beginning of the discharge, but it decays before the end of the discharge. The diamagnetic loop measures the stored energy, the electron temperature and density are measured with a Thomson Scattering system, and the ion temperature is measured by Doppler spectroscopy.  $Z_{eff} \approx 1 - 3$  across much of the plasma column, increasing towards the edge.

## C. V3FIT

The V3FIT code rapidly calculates a simulated magnetic diagnostic signal based on the MHD equilibrium.<sup>25</sup> The pressure profile is modeled by a Lorentz-type expression with two parameters: a scaling factor,  $P_{SCALE}$ , and a shaping parameter,  $AM$ :

$$\frac{p(s)}{P_{SCALE}} = 2(1 + s^{AM})^{-1} - 1, \quad (4)$$

where the radial coordinate is the normalized toroidal flux,  $s = \Phi/\Phi_{LCFS}$ . The enclosed current profile,  $I(s)$ , is modeled by an arctangent function with two parameters: the net current,  $I_{tor}$ , and a shaping parameter,  $AC$ ,

$$I(s) \propto \arctan\left(\frac{ACs^{1.5}}{1-s}\right).$$

The normalization is determined by the total enclosed toroidal current

$$I(s=1) = I_{tor}. \quad (5)$$

V3FIT performs reconstructions of the current and pressure profiles by minimizing the mismatch between the modeled and observed signals,  $S_{m,i}$  and  $S_{o,i}$ , weighted by their respective uncertainty,  $\sigma_i$

$$\chi^2(\mathbf{p}) = \sum_i \left( \frac{S_{o,i} - S_{m,i}(\mathbf{p})}{\sigma_i} \right)^2. \quad (6)$$

During the reconstruction, V3FIT adjusts  $P_{SCALE}$ ,  $AM$ ,  $I_{tor}$ ,  $AC$ , and the net toroidal flux enclosed within the last closed flux surface, i.e.,  $\mathbf{p} = (P_{SCALE}, AM, \dots)$ .

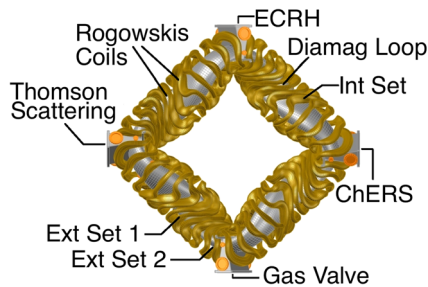


FIG. 2. View of the HSX stellarator (vacuum vessel and field coils) from above with the toroidal locations of the Rogowski coils, diamagnetic flux loop, and the three sets of magnetic diagnostics indicated as shown. Also shown are the locations of the Gas Valve, Thomson Scattering, ECRH, and charge exchange recombination spectroscopy (ChERS, for ion Doppler spectroscopy measurements).



## D. Time evolution of the toroidal current

There is no ohmic current in HSX, so apart from the possibility of an rf-driven current, any net toroidal current is the bootstrap current. During the rapid pressure rise associated with the ECRH and concurrent plasma breakdown, a toroidal electric field is inductively driven by the onset of the non-inductive bootstrap current.

The time evolution of the toroidal current is modeled by solving a 1-D diffusion equation for the rotational transform<sup>13</sup>

$$\frac{d\tau}{dt} = \frac{1}{\Phi_a^2} \frac{d}{ds} \left( \eta_{\parallel} V' \left( \frac{\langle B^2 \rangle}{\mu_0} \frac{d}{ds} (S_{11}\tau + S_{12}) + p'(S_{11}\tau + S_{12}) - \langle \mathbf{J}_{n.i.} \cdot \mathbf{B} \rangle \right) \right). \quad (7)$$

The toroidal current is related to the rotational transform by

$$\tau = \frac{\mu_0 I}{S_{11} \Phi'} - \frac{S_{12}}{S_{11}}. \quad (8)$$

$S_{11}$  and  $S_{12}$  are elements of the susceptance matrix defined in Ref. 13. For a tokamak,  $S_{12} = 0$ , and the vacuum transform is  $\tau = 0$ , but for HSX configurations,  $S_{11}(s) \approx -S_{12}(s) \approx -0.18s$  and  $\tau \approx 1.05 - 1.12$  in vacuum, Fig. 3. The parallel conductivity,  $1/\eta_{\parallel}$ , which is reduced by the trapped particle fraction, is shown in Sec. II D. The plasmas in HSX are low- $\beta$ ; therefore, the  $p'$ -term is small and can be neglected in this calculation. At the center of the plasma column,  $s = 0$ , there is finite current density and the boundary condition is

$$\left. \frac{d\tau}{ds} \right|_{s=0} = 0. \quad (9)$$

At the edge of the plasma column,  $s = 1$ , the measured net toroidal current,  $I(s = 1) = I_{tor}$ , determines the value of  $\tau$  at the edge

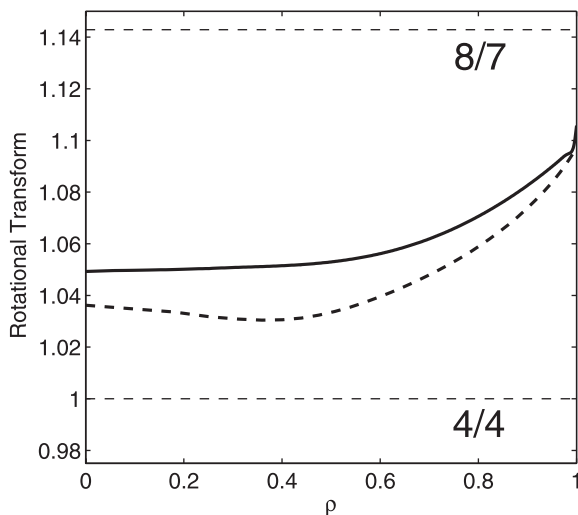


FIG. 3. The rotational transform in vacuum (solid line) and reconstructed profiles at  $t = 50$  ms (dashed line) for the 50 kW on-axis case (discussed below). Low-order rational surfaces relevant to HSX are shown as thin dashed lines.

$$\tau|_{s=1} = \left( \frac{\mu_0 I}{S_{11} \Phi'} - \frac{S_{12}}{S_{11}} \right) \Big|_{s=1}. \quad (10)$$

In Eq. (7),  $\langle \mathbf{J}_{n.i.} \cdot \mathbf{B} \rangle$  can be any non-inductive current source; For HSX, it is the steady-state neoclassical bootstrap current. As described in the Introduction, the neoclassical bootstrap current is calculated by the PENTA code which includes the effects of the conservation of parallel momentum between plasma species and the radial electric field,  $E_r$ .<sup>5,7,8</sup>

The primary effect of the non-axisymmetric shape of the plasma column in HSX, which leads to the non-zero  $S_{12}$ -term in Eq. (7), is to reduce the time for current to diffuse through the plasma column. Two simulations of an ohmically driven plasma current were performed to demonstrate this. The net toroidal current, Eq. (10), was prescribed to ramp from 0 A to 2000 A in 50 ms and then stay constant, Fig 4(a). The parallel conductivity profile of the plasma was  $(4 - 3.99s) \times 10^7$  S/m. The normalized current density profiles for HSX at  $t = (15 \text{ ms}, 50 \text{ ms}, \text{ and } 75 \text{ ms})$  are plotted as solid lines in Fig. 4(b), in blue, red, and black, respectively. The results for an equivalent tokamak (same transform, major and minor radii as HSX) are shown as dashed lines. The normalized steady-state current density profile for the two cases is plotted as a dotted black line. The normalization factor is the current density of the innermost radial point of the simulation domain at steady state,  $J_{\rho \sim 0.1, t=\infty}$ . Here,  $\rho = (\Phi/\Phi_{LCFS})^{1/2}$ . The current diffuses from the edge of the plasma column to the core more rapidly in HSX compared to the tokamak. At  $t = 15$  ms, the current begins to reach the core in the HSX simulation, whereas it is peaked near the edge in the tokamak case. At  $t = 75$  ms, the current density has nearly reached its steady state profile in HSX. At the same time in the tokamak case, the current density near the core has only reached about 50% of its final value. The time required for the current density near the magnetic axis to reach 95% of its steady state value is 84 ms for HSX, while it is 153 ms for the tokamak, nearly a factor of two longer.

Another model for the time evolution of the toroidal current is given in Ref. 14. Assuming an axisymmetric toroidal geometry, the toroidal electric field as a function of radius and time,  $E_T(r, t)$ , is the solution to the following diffusion equation:

$$\mu_0 \sigma_{\parallel} \frac{\partial E_T}{\partial t} = \frac{1}{r} \frac{\partial}{\partial r} \left( r \frac{\partial E_T}{\partial r} \right). \quad (11)$$

The boundary conditions for the decay of the toroidal electric field induced by the bootstrap current, which is relevant for the case of the QHS discharges discussed in this paper, are

$$E_T'(r = 0) = 0, \quad (12)$$

$$E_T(r = a) = -\frac{L_{ext}^* \dot{I}_p}{2\pi R_0}, \quad (13)$$

$$E_T(t = \infty) = 0. \quad (14)$$

Here,  $L_{ext}^* \simeq \mu_0 R_0 (\ln(8R_0/a) - 2)$  is the effective external inductance of a torus with major and minor radii,  $R_0$  and  $a$ . For HSX, the average major and minor radii were used. The

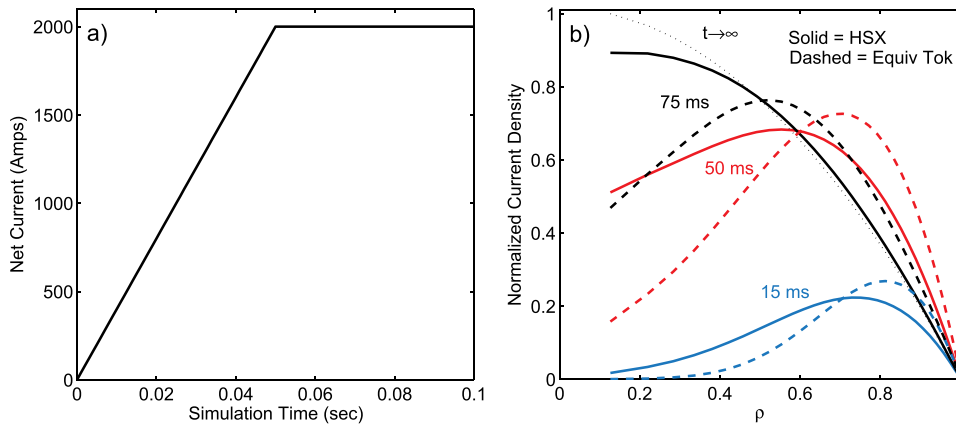


FIG. 4. Ohmic current drive simulation for HSX and an equivalent tokamak: (a) The net induced current and (b) normalized current profiles in HSX (solid lines) and the tokamak (dashed lines). The dotted black line is the steady-state normalized current profile for each case.

conductivity profile,  $\sigma_{||}$ , discussed in Sec. II D, includes corrections due to trapped particle effects. The lowest order eigenvalue of the solution to Eq. (11) corresponds to a current diffusion time of 40–100 ms for the discharges discussed in this paper. However, as stated earlier in this section, the current diffuses about twice as fast in a QHS device compared to an axisymmetric tokamak, reducing the decay time to 20–50 ms. This is consistent with the experimental observation discussed in the next section.

### III. EXPERIMENTAL RESULTS

In this paper, three separate cases are discussed, each with different heating parameters. The first case is with 50 kW of ECRH launched power at an off-axis resonance location,  $\rho \approx 0.3$ . The second case is with 50 kW of ECRH at an on-axis resonance location,  $\rho \leq 0.1$ . The third case is with 100 kW ECRH on-axis,  $\rho \leq 0.1$ . For each case, the ECRH was launched perpendicular to the magnetic axis to minimize electron cyclotron current drive and experiments were performed with the main magnetic field in the clockwise (CW) and counter-clockwise (CCW) direction. For the individual cases, when the field was reversed and other macroscopic plasma parameters were similar (stored energy, density and temperature profiles), all of the magnetic signals were otherwise symmetric with respect to the field reversal. In Fig. 5, the net toroidal current for CW and CCW plasmas is shown for the 50 kW on-axis case. The figure shows that when the field is reversed, the time evolution and steady state estimate of the net toroidal current are very similar. Because of the symmetry of the net current with respect to the reversal of the magnetic field, any ECRH-driven current is assumed to be small. The measurement of the net current in HSX during ECRH indicates that the current is in the direction so as to unwind the transform, as predicted. The energy confinement time of typical plasmas in HSX are in the range of 2–5 ms. Experimental current relaxation times are in the range of 20 ms for off-axis heated plasmas to 50 ms for on-axis heated plasmas, which is consistent with the expected current diffusion time.

Early in the discharge, the net toroidal current is small, and the largest plasma contribution to the measured magnetic fields is due to the Pfirsch-Schlüter current. Reconstructions at  $t = 10$  ms with V3FIT based on the magnetic diagnostics

confirmed that the Pfirsch-Schlüter current is helical and reduced by the high effective transform.<sup>26</sup>

The steady-state estimate of the net toroidal current is plotted versus the measured stored energy for the three heating scenarios in Fig. 6. Keeping the launched power at 50 kW while moving the ECRH resonance from off-axis to on-axis results in roughly doubling both the stored energy and the net toroidal current. The line-averaged density of the off-axis heating case is smaller by 25%. Increasing the launched power from 50 kW to 100 kW while keeping the resonance location fixed on-axis caused the stored energy to rise by approximately 50%, whereas the net toroidal current fell slightly by about 15%. In Fig. 7, we show for comparison the time evolution of the toroidal current for the three nominal discharges that will be analyzed in this paper. For the 50 kW off-axis case, the measured net current nearly reaches steady state before the ECRH power was switched off. The magnetic field is in the clockwise (CW) direction for the off-axis case, but the other two cases have the magnetic field in the counter-clockwise (CCW) direction. More current is measured for the on-axis cases, and the extrapolated steady state current is largest for the 50 kW on-axis

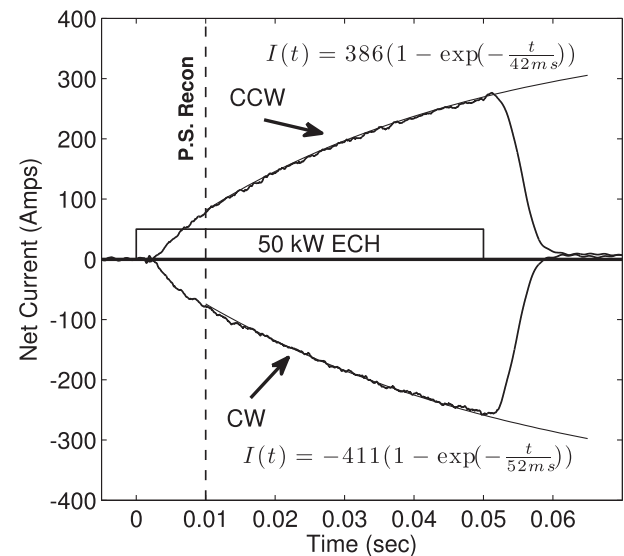


FIG. 5. Measured net toroidal current with the magnetic field in the CCW and CW directions for the 50 kW on-axis heating case. Extrapolated steady state current and decay times are also shown. The reconstruction of the Pfirsch-Schlüter current was performed at  $t = 10$  ms (dashed line).

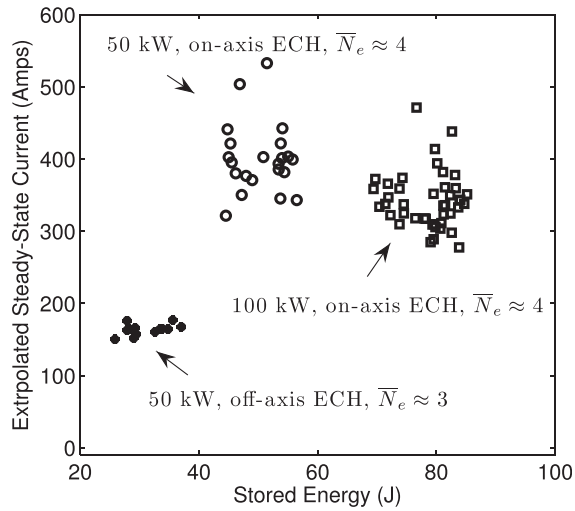


FIG. 6. The extrapolated steady state estimate of the net toroidal current versus the stored energy of the plasma discharge for the three different ECRH conditions.

case. In the discussion below, the directional dependence of the magnetic field is removed to simplify comparison, unless otherwise noted.

### A. Bootstrap current

Profiles of  $T_e$ ,  $T_i$ , and  $N_e$  for the three different ECRH cases are shown in Figs. 8 and 9. The main difference between the  $T_e$  profiles is in the peaking of the profile inside of  $\rho \sim 0.4$ . The central electron temperature drops as low as 400 eV for the off-axis heating case and increases up to 1600 eV for 100 kW on-axis ECRH. In each case, the profiles were used as input to the PENTA code to calculate the ambipolar  $E_r$  solutions, the corresponding electron and ion bootstrap current densities,  $J_{b,e}$  and  $J_{b,i}$  and the total bootstrap current density,  $J_b = J_{b,e} + J_{b,i}$ . These values were calculated both with and without the effects of momentum conservation between the electrons and ions in the parallel flow. Figs. 10(a)–10(c) show the radial electric field for the three heating cases, the black (red) curves indicate the solution with (without) momentum conservation.

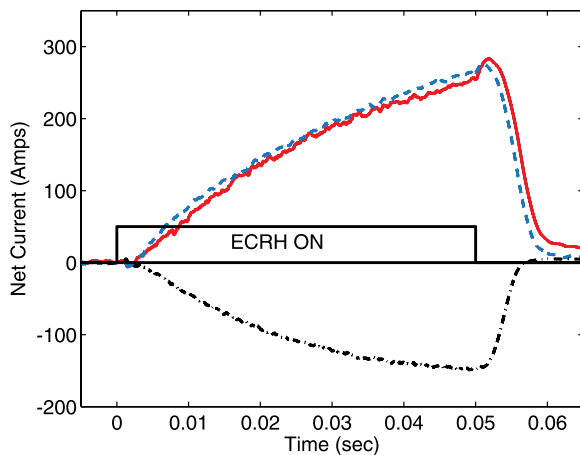


FIG. 7. The measured net toroidal current for the three different ECRH conditions: CW 50 kW off-axis (black, dashed-dotted), CCW 50 kW on-axis (blue, dashed), and CCW 100 kW on-axis (red, solid).

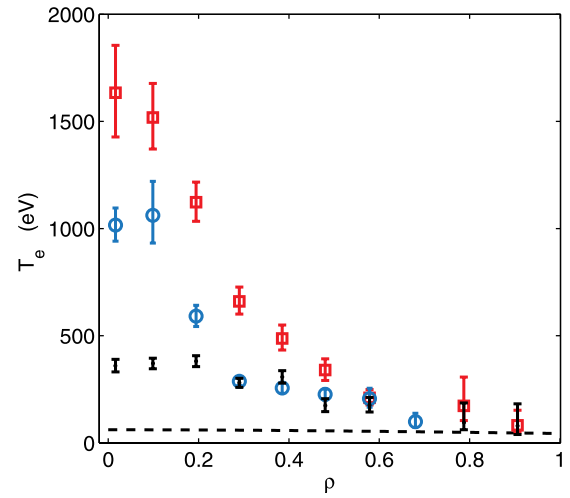


FIG. 8.  $T_e$  for 50 kW ECRH off-axis (black points), 50 kW ECRH on-axis (blue circles) and 100 kW ECRH on-axis (red squares).  $T_i$  from Doppler spectroscopy (black, dashed).

In the 50 kW off-axis case, Fig. 10(a), only one ambipolar  $E_r$  root, the “ion-root,” is stable across the entire plasma column. In the 50 kW on-axis case, Fig. 10(b), the ion-root remains a stable solution across most of the plasma column. An additional stable  $E_r$  solution, the “electron-root” exists near the magnetic axis, characterized by a much larger  $E_r$  than the ion-root solution. It is indicated by dashed lines in the figure. In the momentum conserving case, there is a small region near the axis,  $\rho < 0.12$ , in which there is only an electron-root solution and no ion-root solution. With 100 kW on-axis heating, Fig. 10(c), the electron-root regions are 75 V/cm higher in magnitude and extend to a slightly larger radius. The region near the axis, which has only an electron-root is larger,  $\rho < 0.16$ , and exists both with and without momentum conservation. The values of  $E_r$  are 20–30 V/cm larger with momentum conservation included in the calculation.

While the profiles of  $E_r$  are similar with and without momentum conservation, the predicted individual electron and ion bootstrap current densities show a dependence on

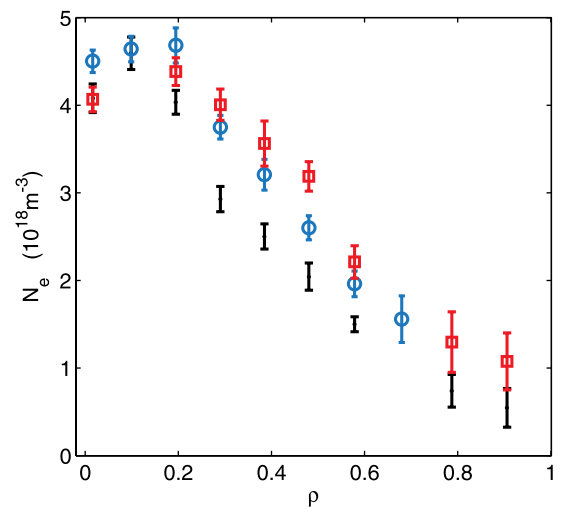


FIG. 9.  $N_e$  for 50 kW ECRH off-axis (black points), 50 kW ECRH on-axis (blue circles) and 100 kW ECRH on-axis (red squares).

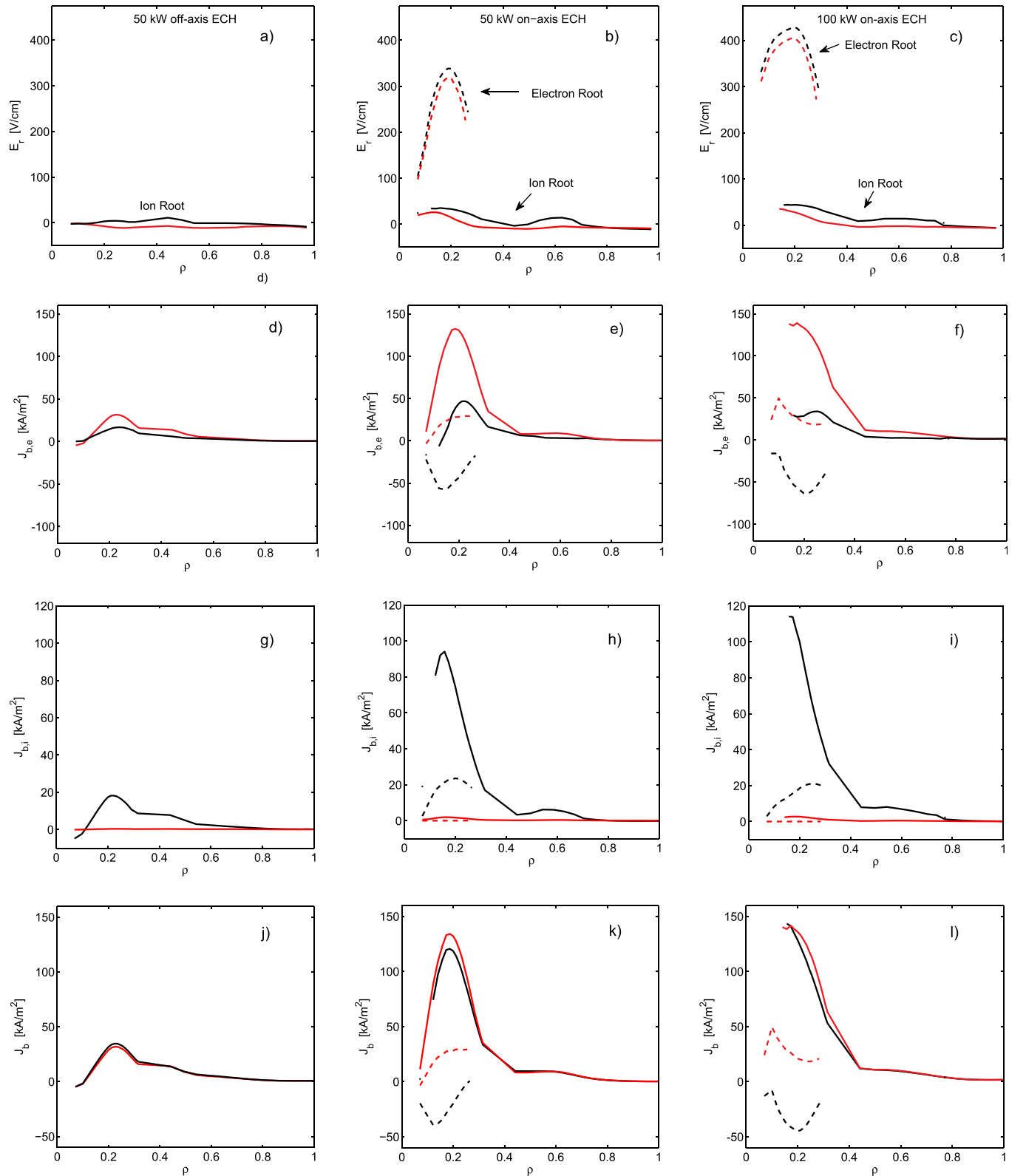


FIG. 10.  $E_r$ ,  $J_{b,e}$ ,  $J_{b,i}$ , and  $J_b$  for 50 kW ECRH off-axis (left), 50 kW ECRH on-axis (center) and 100 kW ECRH on-axis (right). Calculations with (without) momentum conservation shown in black (red). Ion-root (electron-root) solution shown as solid (dashed) lines.

the inclusion of momentum conservation, particularly near the magnetic axis  $\rho \leq 0.5$ , Figs. 10(d)–10(i). However, the total bootstrap current, Figs. 10(j)–10(l), show a strong dependence only in the electron-root solution.

$J_{b,e}$  for the three heating cases is shown in Figs. 10(d)–10(f). The black (red) curves indicate that momentum

conservation is included (neglected) from the calculation. Solid (dashed) curves represent the ion-root (electron-root) solutions. For each of the individual cases,  $J_{b,e}$  profiles are similar to each other from the mid-radius to the edge,  $\rho \geq 0.5$ , whether or not momentum conservation is included in the calculation. Significant differences between the two



calculations of the electron current density exist at radii closer to the magnetic axis. In each heating case  $J_{b,e}$  in the ion-root is larger near the magnetic axis when momentum conservation is not included compared to when it is included. The factor is about  $2\times$  in the 50 kW off-axis case, Fig. 10(d), and increases to about  $4\times$  in the 100 kW on-axis case, Fig. 10(f). When the electron-root exists,  $J_{b,e}$  reverses direction and is reduced in magnitude with momentum conservation, Figs. 10(e)–10(f). Without momentum conservation,  $J_{b,e}$  is reduced in magnitude but does not reverse direction.

The profiles of  $J_{b,i}$  are shown in Figs. 10(g)–10(i). The same color scheme is followed as for  $J_{b,e}$ . When momentum conservation is neglected,  $J_{b,i}$  is relatively small, both in the ion- and electron-roots. Momentum between the electrons and ions is not exchanged and the ion flow has little to no driving force. With the inclusion of momentum conservation,  $J_{b,i}$  is on the same order of magnitude as  $J_{b,e}$ .  $J_{b,i}$  in the ion-root increases as the heating is moved from off- to on-axis (at fixed power), and as the heating power is increased from 50 kW to 100 kW (at fixed resonance location). In the electron root,  $J_{b,i}$  is reduced significantly, although it does not reverse direction.

The total bootstrap current density,  $J_b$ , is shown in Figs. 10(j)–10(l). For each of the cases,  $J_b$  in the ion-root is similar regardless of whether or not momentum conservation is included. Some of the current that is carried by the electrons in the non-momentum conserving calculation is carried by the ions in the momentum conserving calculation, so while the individual electron and ion current densities are quite different with or without momentum conservation, the total current densities are very similar,  $J_{b,ion-root,MC} \approx J_{b,ion-root,non-MC}$ . In the electron-root,  $J_b$  reverses direction when momentum conservation is included. Without momentum conservation,  $J_b$  is simply reduced in magnitude.

The calculated total volume integrated bootstrap current,  $I_b = \int_0^1 ds J_b(s)$ , is shown in Table I and compared to the extrapolated steady state value of the measured current,  $I_{tor}(t = \infty)$ . For this integration,  $J_b(s = 0) \equiv 0$  and  $J_b$  is linearly interpolated (in  $s$ ) for  $0 < \rho < 0.08$  ( $0 < s < 0.28$ ). When there are multiple solutions to the ambipolarity constraint, it is necessary to account for the coupling between flux surfaces with a diffusion equation for the radial electric field (see Ref. 8 and references therein). As shown in Fig. 6(a) of Ref. 8, the  $E_r$  profile is strongly dependent on the value of the diffusion coefficient. Lacking experimental data to validate a particular value for the diffusion coefficient, in this paper, we will instead bracket the calculated value of the bootstrap current. Close to the core, the e-root only region for the 100 kW on-axis case adds little to the integrated current because of the negligible volume. Outside this region,

we consider two limiting cases that provide an upper and lower bound to the bootstrap current. This is analogous to having a high or low value for the electric field diffusion coefficient. The first limit is with the integrand equal to the current density of the ion-root electric field solution. This limit is indicated by “i-root.” The other limit is with the integrand equal to the current density of the electron-root solution, indicated by “e-root.” The spread in the extrapolated steady state value represents the standard deviation of the individual fits. We estimate, using a Monte Carlo analysis, an approximately 10% error in the calculated bootstrap current due to the uncertainty in the measured electron temperature and density profiles.

There is only one i-root solution for the 50 kW off-axis heating scenario, and the estimates of the total current with and without momentum conservation agree to within 10%. The on-axis heated scenarios each have regions of e-root solutions near the magnetic axis. With the ECRH location fixed on-axis, raising the launched power from 50 kW to 100 kW raises the i-root limit from 488 A to 580 A, whereas the e-root limit stays almost constant near 202 A when momentum conservation is included. Without momentum conservation, both the i-root and e-root limits rise, the former from 537 A to 698 A and the latter from 333 A to 436 A.

The experimental extrapolated steady state values are also shown in the table. For the 50 kW off-axis case, the measured value is smaller than both calculations by 60–80 A, or 30%. For the 50 kW on-axis case, the measured value is between the ion-root and electron-root limits, both with and without momentum conservation,  $I_{b,e-root} < I_{tor}(t = \infty) < I_{b,i-root}$ , suggesting that some part of the core of the plasma has  $E_r$  in the electron-root. For the 100 kW on-axis case, the measured value is between the ion-root and electron-root limits when momentum conservation is included. Again, this suggests part of the plasma near the axis is in the electron-root. If momentum conservation is neglected, the ion-root limit is nearly double the measured value and the electron-root limit exceeds the measurement by about 90 A. When momentum conservation is neglected, the calculation is not consistent with the measurement, in either limit. These results are summarized in Fig. 11 where the range of ( $I_{b,e-root}$ ,  $I_{b,i-root}$ ) is shown in gray (red) when momentum conservation is included (neglected). The extrapolated steady-state values of the net current (from Fig. 6) are repeated for reference.

## B. Time evolution

The parallel electrical conductivity including the effects of trapped particles,  $\sigma_{\parallel} \equiv \eta_{\parallel}^{-1}$ , for the three heating cases is

TABLE I. The three ECRH scenarios arranged by launched power and resonance location. The extrapolated steady state current and the calculated net bootstrap current with and without momentum conservation in ion-root and electron-root limits are shown.

Heating scenario	$I_{tor}(t = \infty)$	$I_b$ , w/ MC, i-root	$I_b$ , w/ MC, e-root	$I_b$ , w/o MC, i-root	$I_b$ , w/o MC, e-root
50 kW off-axis	$166 \pm 13$ A	248 A	-	229 A	-
50 kW on-axis	$399 \pm 35$ A	488 A	202 A	537 A	333 A
100 kW on-axis	$348 \pm 21$ A	580 A	204 A	698 A	436 A

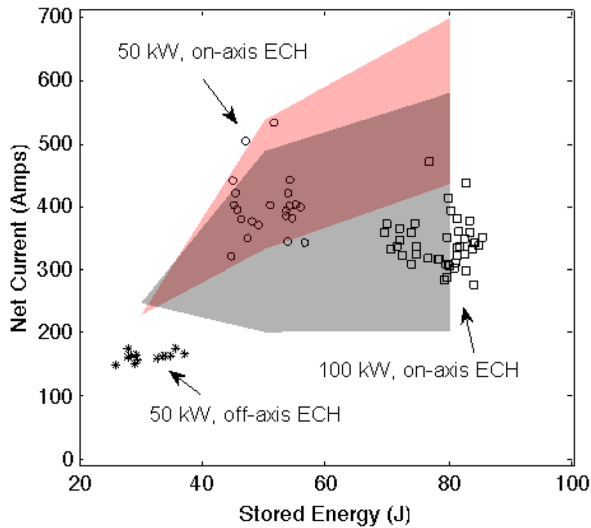


FIG. 11. The extrapolated steady state estimate of the net toroidal current versus the stored energy of the plasma discharge for the three different ECRH conditions, along with the limits of the  $I_{b,e-root}$  and  $I_{b,i-root}$  with MC (grey) and without MC (red).

shown in Fig. 12. The conductivity is primarily a function of  $T_e^{(3/2)}$ ; it is lowest for the 50 kW off-axis case and is largest for the 100 kW on-axis case.

For each of the heating scenarios, the profiles of  $\sigma_{||}$ , the measured net toroidal current, and the calculated  $J_b$  profiles are used in Eq. (7) to determine the time evolution of  $t$  and the current profile. The  $J_b$  profiles selected include momentum conservation and use the ion-root solution whenever multiple roots to the ambipolarity constraint exist,  $J_b = J_{b,ion-root,MC}$ . The simulated radial profiles of the induced toroidal current density at 10 ms and 50 ms are shown in Figs. 13(a)–13(c). In each simulation, the induced current decays from 10 ms to 50 ms.

### C. V3FIT equilibrium reconstructions

Reconstructions of the plasma pressure and current profiles were performed for each of the three cases discussed above. Since the results are similar for the three cases, we will show only one case here, specifically the 50 kW on-axis heating scenario. When a Rogowski coil, the external magnetic diagnostics (Poloidal Indices 1–32), and the location of

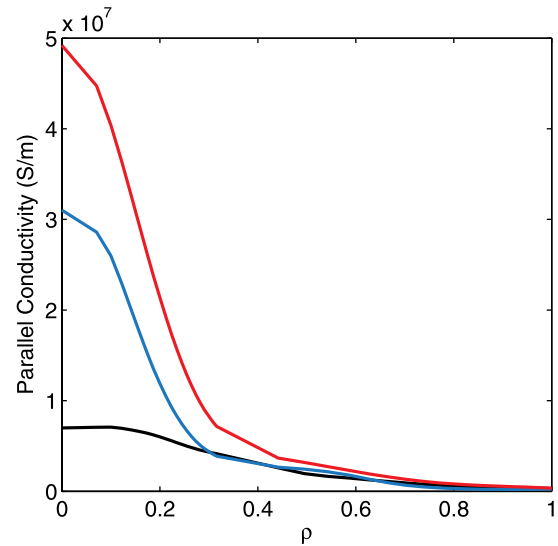


FIG. 12. Parallel electrical conductivity,  $\sigma_{||}$ , for 50 kW ECRH off-axis (black), 50 kW ECRH on-axis (blue), and 100 kW ECRH on-axis (red).

an edge limiter were used as constraints for the reconstruction, the reconstructed pressure profile was larger than the profile measured by the Thomson Scattering system. This reconstruction is shown in Fig. 14. The total stored energy in the reconstruction is about two to three times that which is measured from integration of the kinetic measurements as well as from the diamagnetic loop. The presence of eddy current in the vacuum vessel is the likely cause of the discrepancy. The eddy currents have not been modeled at this point.

When the internal Rogowski coil, the internal magnetic diagnostics (Poloidal Indices 33–47), and the position of an edge limiter were used as constraints for the reconstruction calculation, the plasma pressure and current profiles at  $t=50$  ms are then in good agreement with Thomson Scattering and the simulated current, respectively. This is shown in Figs. 15(a) and 15(b). The simulated current profile is the evolved current profile using the  $J_b = J_{b,ion-root,MC}$  profile discussed above. An arctangent function fitted to this current profile (not shown) serves as the initial profile for the reconstruction.

The magnetic signals for the reconstructed profiles and the measured data are shown in Fig. 15(c). The V3FIT

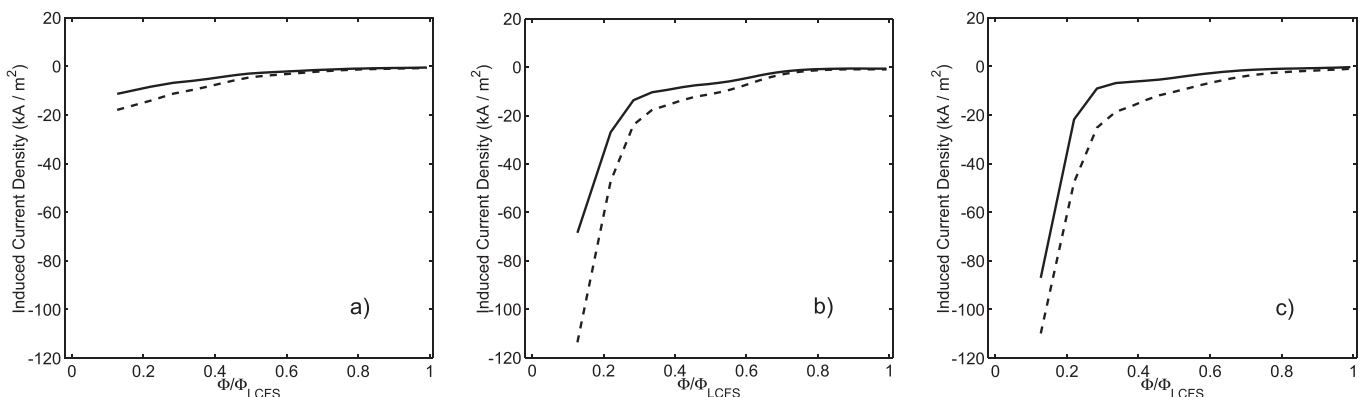


FIG. 13. Simulated induced current profiles at  $t=10$  ms (dashed lines) and  $t=50$  ms (solid lines) for (a) 50 kW ECRH off-axis, (b) 50 kW ECRH on-axis, and (c) 100 kW ECRH on-axis (right).

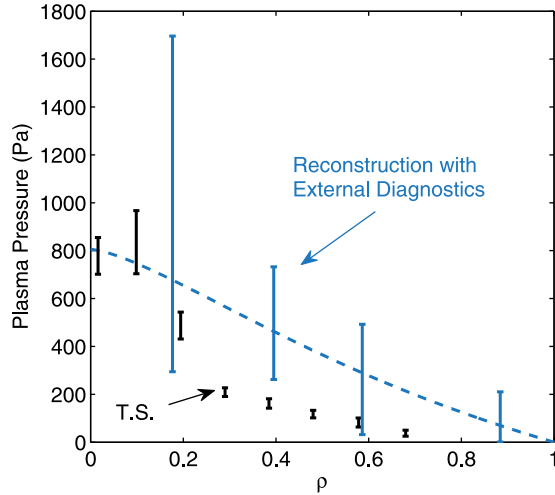


FIG. 14. The measured plasma pressure profile based on Thomson Scattering and Doppler spectroscopy (black points and error bars) and the reconstructed pressure profile using external diagnostics as constraints for the 50 kW ECRH on-axis case (blue dashed lines with error bars).

reconstruction minimizes the mismatch between the modeled and observed signals, and  $\chi^2$  is reduced from 13.1 to 4.2. The reconstructed  $t$  profile is shown in Fig. 3. Major low-order resonances are avoided.

After the reconstruction was completed, the pressure profile was varied by adjusting the pressure parameters (i.e.,  $P_{SCALE}$  and  $AM$ ) while holding the parameters of the current profile and net toroidal flux at their reconstructed values and calculating  $\chi^2_\nu = \chi^2/\nu$ , where  $\nu = n - m - 1$ ,  $n = 17$  is the total number of constraints and  $m = 5$  is the number of free parameters. The process was repeated for the current profile, while keeping the pressure parameters and flux at their reconstructed values. In this context, profiles that satisfy

$$\chi^2_\nu \leq \chi^2_{\nu, \min} + 1 \quad (15)$$

are considered to fall within a single standard deviation interval of the reconstructed solution. For the pressure profiles, the edge profiles are fairly well constrained, while the core of the plasma has larger uncertainties. For the current profile, the uncertainties are large for  $\rho < 0.5$ , and details of the current density profile,  $J_b \propto \frac{d}{d\rho} I_{enclosed}$ , cannot be resolved

by reconstructions performed with the existing magnetic diagnostic array as constraints.

#### IV. SUMMARY AND DISCUSSION

The bootstrap current was analyzed for three scenarios of ECRH in the quasihelically symmetric HSX. For all three cases, it was verified that the current flowed in a direction so as to unwind the transform, in agreement with theoretical predictions and opposite to what occurs in a tokamak. For an ensemble of discharges, the extrapolated steady-state current was observed to increase in stored energy and total current when the heating location was moved from off-axis to on-axis with 50 kW heating power. However, when the on-axis heating power was increased from 50 kW to 100 kW, the stored energy continued to increase while the bootstrap current decreased slightly. This measurement is qualitatively consistent with the calculations of the bootstrap current by PENTA code when momentum conservation is included in the calculation,  $I_{b, meas} \approx I_{b, M.C.}$  or  $I_{b, e-root M.C.} \leq I_{b, meas} \leq I_{b, i-root M.C.}$ . Without momentum conservation, the calculated steady-state bootstrap current increases monotonically, which is contradicted by the experimental data. PENTA calculates that a large positive radial electric field, the electron root to the ambipolarity constraint, should exist close to the magnetic axis for the on-axis heating cases and that this  $E_r$  acts to reverse the direction of the current in that location and decreases the total integrated current. This mechanism could explain the decrease in  $I_{tor}(t = \infty)$  with increasing ECRH power. However, data from Charge Exchange Recombination Spectroscopy (ChERS)<sup>27</sup> shows no indication of such a large radial electric field, although this measurement is unable to adequately resolve the magnitude of the radial electric field very close to the magnetic axis because of the finite width of the neutral beam that is employed.

While the scaling of the calculated bootstrap current qualitatively agrees with the measurements, the details of the e-root/i-root transition have not been well modeled. One difficulty is that when there are regions of high positive electric field next to regions of much lower electric field, there is a very sharp gradient in the plasma flow which is unphysical.

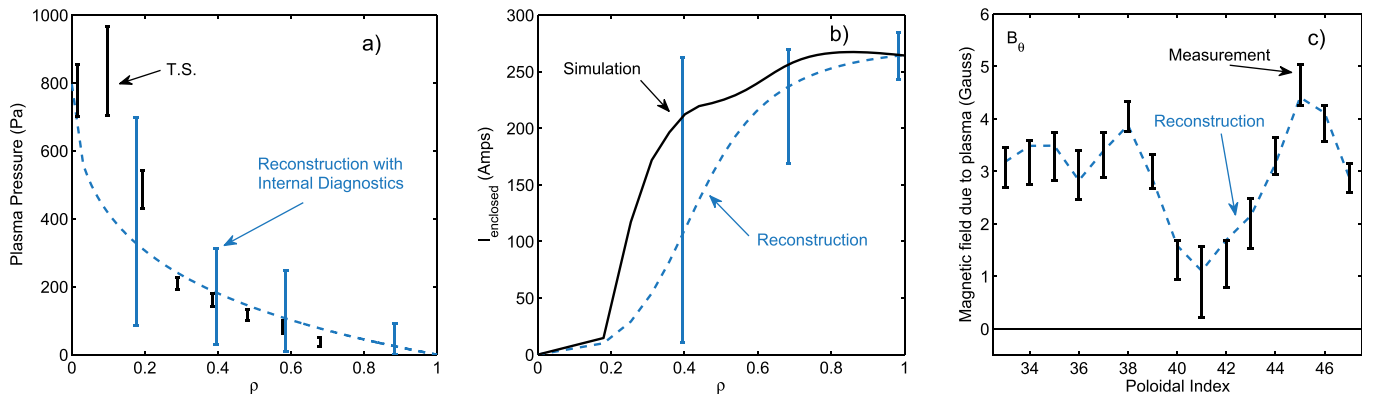


FIG. 15. (a) Measured (black points with error bars) and reconstructed (blue dashed line) plasma pressure profiles. (b) Simulated (black solid line) and reconstructed (blue dashed line) enclosed current profiles at  $t = 50$  ms. (c) Measured magnetic diagnostic signals with uncertainties (black points with error bars) and calculated signals of the reconstructed profiles (blue dashed lines).

In that case, a diffusion equation for the electric field needs to be solved and this equation is parameterized by a diffusion coefficient  $D_E$  related to the perpendicular viscosity.<sup>28</sup> The difficulty with finding the electric field profile numerically with a diffusion equation is assuming whether the value of  $D_E$  should be set by neoclassical values or from turbulence. Without experimental measurements of the radial electric field close to the magnetic axis, it is difficult to benchmark the value of  $D_E$  and often a range of values is assumed<sup>8</sup> in a calculation.

Another limitation in the modeling is that the assumptions that underlie the DKES calculations, and hence the PENTA modification, may be invalid for the two on-axis heating cases. The poloidal component of the drift velocity vanishes at the resonant electric field, given by  $E_{res} = (|m - nq|/m)v_T B_p$ ,<sup>29</sup> where  $v_T$  is the ion thermal velocity. The ion flux sharply increases at  $E_{res}$  and then decreases rapidly above this electric field. This resonance is responsible for the calculated electron root for HSX plasmas.<sup>8</sup> For tokamaks and most stellarators dominated by toroidal curvature, the  $n=0$ ,  $m=1$  toroidal resonance is most important. For HSX, however, the  $n=4$ ,  $m=1$  term in the magnetic spectrum dominates so that the resonant electric field in HSX is about 3 times higher (with  $q \sim 1$ ) than a stellarator with the same rotational transform. Calculations that compared the results of a  $\delta f$ -Monte Carlo code to the DKES indicate that close to the resonance the  $E \times B$  drift can no longer be assumed to be incompressible.<sup>30</sup> The incompressible assumption allows for a monoenergetic treatment of the drift kinetic equation for the DKES code. The  $\delta f$  calculations show that the kinetic energy is not conserved close to the resonance and that the monoenergetic approximation should be limited to electric field such that  $E_r < 0.5 - 0.7 \times E_{res}$ . Further work estimating what effect the DKES monoenergetic approximation has on the PENTA calculations is beyond the scope of this paper, but it may indicate a limitation on the applicability of the momentum correction approach based on the DKES database.

For the 50 kW off-axis case, in which the ion root electric field is far from the resonance electric field, the assumptions in the DKES code remain valid, but the calculated total bootstrap current overestimates the measured bootstrap current by about 60–80 A, or 30%.

For each case, the Pustovitov-Shafranov and Strand-Houlberg model of the current evolution was applied to calculate the time evolution of the current profile. This 3D model couples the toroidal and poloidal fluxes through the  $S_{12}$  term of Eq. (7). There is no coupling between the poloidal and toroidal fluxes in a 2D axisymmetric current diffusion equation,  $S_{12} = S_{21} = 0$ . Simulations of current drive in HSX and an equivalent tokamak show that the current diffuses into the plasma column nearly twice as fast in HSX than in the tokamak.

Using the V3FIT code, reconstructions of the plasma pressure and current profiles were performed using a Rogowski coil and either a set of 32 magnetic coils located outside the vacuum chamber or a set of 15 coils inside the chamber. With the external coils, there is a factor of 2–3 difference between the stored energy from the integrated

reconstructed pressure profile and the Thomson scattering measurements. Using the interior coils, the agreement between the reconstruction and the measured pressure profile was much improved and good agreement was found between calculated and reconstructed current profiles. The difference in the reconstructions using internal versus external sensors is suspected to be due to induced eddy currents in the stainless steel vacuum vessel. The uncertainties in the pressure and current profiles are largest near the core of the plasma, while the edge profiles are well-constrained.

Only limited details of the pressure and current profiles can be determined from magnetics data for axisymmetric devices.<sup>31</sup> More information can be extracted from the magnetic field exterior to the plasma column for a 3-D device, provided that the signal-to-noise ratio of the sensors is sufficiently high and that the placement of the magnetic sensors are optimized to spatially sample the surrounding magnetic field in specific locations.<sup>32,33</sup> Even with these improvements in the measurements, relying solely on magnetics for equilibrium reconstruction may be insufficient to resolve details of the profiles far from the diagnostics (close to the magnetic axis).<sup>34</sup> Including additional diagnostic data (i.e., Thomson scattering, interferometry) as constraints for the reconstruction will further improve reconstructions of the plasma column shape, pressure and current profiles.<sup>16</sup>

## ACKNOWLEDGMENTS

Much gratitude and good thoughts in memory of Mike Frankowski, who always gave thoughtful advice throughout the years. Special thanks go to Paul Probert for the construction of the prototype external magnetic diagnostic system. This work was supported by DOE Grant DE-FG02-93ER54222.

- <sup>1</sup>C. D. Beidler, M. Yu. Isaev, S. V. Kasilov, W. Kernbichler, H. Maaßberg, D. R. Mikkelsen, S. Murakami, V. V. Nemov, M. Schmidt, D. A. Spong, V. Tribaldos, and A. Wakasa, *22nd IAEA Fusion Energy Conference, TH/P8-10, IAEA, Geneva, 2008*.
- <sup>2</sup>J. Geiger, C. D. Beidler, M. Drevlak, H. Maaßberg, C. Nührenberg, Y. Suzuki, and Y. Turkin, *Contrib. Plasma Phys* **50**, 770 (2010).
- <sup>3</sup>W. I. van Rij and S. P. Hirshman, *Phys. Fluids B* **1**, 563 (1989).
- <sup>4</sup>M. Taguchi, *Phys. Fluids B* **4**, 3638 (1992).
- <sup>5</sup>H. Sugama and S. Nishimura, *Phys. Plasmas* **9**, 4637 (2002).
- <sup>6</sup>H. Maaßberg, C. D. Beidler, and Y. Turkin, *Phys. Plasmas* **16**, 072504 (2009).
- <sup>7</sup>D. A. Spong, *Phys. Plasmas* **12**, 056114 (2005).
- <sup>8</sup>J. Lore, W. Guttenfelder, A. Briesemeister, D. T. Anderson, F. S. B. Anderson, C. B. Deng, K. M. Likin, D. A. Spong, J. N. Talmadge, and K. Zhai, *Phys. Plasmas* **17**, 056101 (2010).
- <sup>9</sup>N. Nakajima, M. Okamoto, and M. Mujiwara, "Physical Mechanism of  $E_\psi$ -Driven Current in Asymmetric Toroidal Systems," National Institute for Fusion Science, NIFS-172, NIFS, 1992).
- <sup>10</sup>K. Y. Watanabe, N. Nakajima, M. Okamoto, K. Yamazaki, Y. Nakamura, and M. Wakatani, *Nucl. Fusion* **35**, 335 (1995).
- <sup>11</sup>G. Motojima, K. Nagasaki, H. Okada, K. Watanabe, T. Mizuuchi, A. Matsuyama, K. Hanatani, S. Yamamoto, S. Kobayashi, Y. Suzuki, K. Kondo, Y. Nakamura, A. C. Fernández, Á. A. Cappa, Y. Yoshimura, S. Watanabe, K. Mukai, and F. Sano, *J. Plasma Fusion Res.* **8**, 1010 (2009).
- <sup>12</sup>V. D. Pustovitov and V. D. Shafranov, *Rev. Plasma Phys.* **15**, 163 (1990).
- <sup>13</sup>P. I. Strand and W. A. Houlberg, *Phys. Plasmas* **8**, 2782 (2001).
- <sup>14</sup>D. R. Mikkelsen, *Phys. Fluids B* **1**, 333 (1989).
- <sup>15</sup>L. L. Lao, J. R. Ferron, R. J. Groebner, W. Howl, H. St. John, E. J. Strait, and T. S. Taylor, *Nucl. Fusion* **30**, 1035 (1990).

- <sup>16</sup>J. D. Hanson, D. T. Anderson, M. Cianciosa, P. Franz, J. H. Harris, G. H. Hartwell, S. P. Hirshman, S. F. Knowlton, L. L. Lao, E. A. Lazarus, L. Marrelli, D. A. Maurer, J. C. Schmitt, A. C. Sontag, B. A. Stevenson, and D. Terranova, *Nucl. Fusion* **53**, 083016 (2013).
- <sup>17</sup>M. C. Zarnstorff, A. Weller, J. Geiger, E. Fredrickson, S. Hudson, J. P. Knauer, A. Reiman, A. Dinklage, G.-Y. Fu, L. P. Ku, D. Monticello, and A. Werner, 20th IAEA Fusion Energy Conference, EX/3-4 (IAEA, Vilamoura, 2004).
- <sup>18</sup>J. D. Hanson, S. P. Hirshman, S. F. Knowlton, L. L. Lao, E. A. Lazarus, and J. M. Shields, *Nucl. Fusion* **49**, 075031 (2009).
- <sup>19</sup>S. P. Hirshman and J. C. Whitson, *Phys. Fluids* **26**, 3553 (1983).
- <sup>20</sup>F. S. B. Anderson, A. F. Almagri, D. T. Anderson, P. G. Matthews, J. N. Talmadge, and J. L. Shohet, *Fusion Technol.* **27**, 273 (1995).
- <sup>21</sup>A. H. Boozer, *Phys. Fluids* **25**, 520 (1982).
- <sup>22</sup>J. N. Talmadge, V. Sakaguchi, F. S. B. Anderson, and A. F. Almagri, *Phys. Plasmas* **8**, 5165 (2001).
- <sup>23</sup>A. H. Boozer, *Phys. Fluids* **24**, 1999 (1981).
- <sup>24</sup>A. H. Boozer and H. J. Gardner, *Phys. Fluids B* **2**, 2408 (1990).
- <sup>25</sup>S. P. Hirshman, E. A. Lazarus, J. D. Hanson, S. F. Knowlton, and L. L. Lao, *Phys. Plasmas* **11**, 595 (2004).
- <sup>26</sup>J. C. Schmitt, J. N. Talmadge, and D. T. Anderson, *Nucl. Fusion* **53**, 082001 (2013).
- <sup>27</sup>A. Briesemeister, K. Zhai, D. T. Anderson, F. S. B. Anderson, and J. N. Talmadge, *Plasma Phys. Controlled Fusion* **55**, 014002 (2013).
- <sup>28</sup>K. C. Shaing, *Phys. Fluids* **27**, 1567 (1984).
- <sup>29</sup>K. C. Shaing, *Phys. Fluids B* **5**, 3841 (1993).
- <sup>30</sup>C. D. Beidler, J. Geiger, H. Maaßberg, N. B. Marushchenko, Yu. Turkin, and W7-AS Team, in *Proceedings of the 17th International Toki Conference and 16th International Stellarator/Heliotron Workshop, Toki, 2007 NIFS-PROC Series Research Report* (Toki, 2007), p. 623.
- <sup>31</sup>L. L. Lao, H. St. John, R. D. Stambaugh, and W. Pfeiffer, *Nucl. Fusion* **25**, 1421 (1985).
- <sup>32</sup>N. Pomphrey, E. Lazarus, M. Zarnstorff, A. Boozer, and A. Brooks, *Phys. Plasmas* **14**, 056103 (2007).
- <sup>33</sup>J. Geiger, M. Ender, and A. Werner, *Contrib. Plasma Phys.* **50**, 736 (2010).
- <sup>34</sup>V. D. Pustovitov, *Nucl. Fusion* **41**, 721 (2001).